ENSO and Wintertime Extreme Precipitation Events over the Contiguous United States

SIEGFRIED D. SCHUBERT, YEHUI CHANG,* MAX J. SUAREZ, AND PHILIP J. PEGION+

Global Modeling and Assimilation Office, Earth–Sun Exploration Division, NASA GSFC, Greenbelt, Maryland

(Manuscript received 29 September 2006, in final form 3 April 2007)

ABSTRACT

In this study the authors examine the impact of El Niño–Southern Oscillation (ENSO) on precipitation events over the continental United States using 49 winters (1949/50–1997/98) of daily precipitation observations and NCEP–NCAR reanalyses. The results are compared with those from an ensemble of nine atmospheric general circulation model (AGCM) simulations forced with observed SST for the same time period. Empirical orthogonal functions (EOFs) of the daily precipitation fields together with compositing techniques are used to identify and characterize the weather systems that dominate the winter precipitation variability. The time series of the principal components (PCs) associated with the leading EOFs are analyzed using generalized extreme value (GEV) distributions to quantify the impact of ENSO on the intensity of extreme precipitation events.

The six leading EOFs of the observations are associated with major winter storm systems and account for more than 50% of the daily precipitation variability along the West Coast and over much of the eastern part of the country. Two of the leading EOFs (designated GC for Gulf Coast and EC for East Coast) together represent cyclones that develop in the Gulf of Mexico and occasionally move and/or redevelop along the East Coast producing large amounts of precipitation over much of the southern and eastern United States. Three of the leading EOFs represent storms that hit different sections of the West Coast (designated SW for Southwest coast, WC for the central West Coast, and NW for northwest coast), while another represents storms that affect the Midwest (designated by MW). The winter maxima of several of the leading PCs are significantly impacted by ENSO such that extreme GC, EC, and SW storms that occur on average only once every 20 years (20-yr storms) would occur on average in half that time under sustained El Niño conditions. In contrast, under La Niña conditions, 20-yr GC and EC storms would occur on average about once in 30 years, while there is little impact of La Niña on the intensity of the SW storms. The leading EOFs from the model simulations and their connections to ENSO are for the most part quite realistic. The model, in particular, does very well in simulating the impact of ENSO on the intensity of EC and GC storms. The main model discrepancies are the lack of SW storms and an overall underestimate of the daily precipitation variance.

1. Introduction

Global-scale climate variations such as those associated with El Niño–Southern Oscillation (ENSO) are ultimately manifest in phenomena and processes that control regional-scale climates. For example, shifts in the wintertime planetary-scale waves forced by tropical sea surface temperature (SST) anomalies can result in changes in the normal tracks and frequencies of storm systems (e.g., Noel and Changnon 1998) which can result in dramatic changes in regional climates of North America. There is considerable evidence that precipitation along the Pacific coast of North America is impacted by ENSO (e.g., Schonher and Nicholson 1989) and various other large-scale modes of variability such as the Pacific–North American (PNA) pattern (e.g., Yarnal and Diaz 1986), the Madden–Julian oscillation (e.g., Mo and Higgins 1998), and a 20–25-day oscillatory mode (Mo 1999). During the warm season, changes in

* Additional affiliation: Goddard Earth Sciences and Technology Center, University of Maryland, Baltimore County, Baltimore, Maryland.

+ Additional affiliation: Science Applications International Corporation, Beltsville, Maryland.

Corresponding author address: Siegfried D. Schubert, Global Modeling and Assimilation Office, Earth–Sun Exploration Division, NASA GSFC, Greenbelt, MD 20771.
E-mail: siegfried.d.schubert@nasa.gov

DOI: 10.1175/2007JCLI1705.1

the strength or position of the oceanic subtropical highs can, for example, lead to changes in the normal influx of water into the United States from the Gulf of Mexico that in turn influences developing mesoscale and larger storm systems (e.g., Helfand and Schubert 1995; Higgins et al. 1997; Schubert et al. 1998).

Any potential changes in extreme weather events are of particular concern since these tend to have the greatest economic and social consequences. It is therefore of interest to determine whether the characteristics of extreme events are influenced by short-term climate variability (e.g., ENSO) as well as by longer-term climate change (Houghton et al. 2001). Zwiers and Kharin (1998), for example, analyzed CO_2-doubling experiments with a coupled general circulation model and found an increase in precipitation extremes almost everywhere over the globe. Gershunov and Barnett (1998) and Gershunov (1998) show that the frequency of heavy rainfall is impacted by ENSO in a number of regions of the United States including the Great Plains, the Southeast, and the Gulf States. Cayan et al. (1999) show that ENSO impacts the occurrence of extreme (heavy) daily precipitation and streamflow throughout the western United States.

One limitation of many recent studies of weather extremes is that the analysis of the extreme events is carried out locally in space, with little information provided about the underlying phenomenology and mechanisms associated with the extremes. In the case of precipitation, Webb and Betancourt (1992) emphasize that understanding the hydroclimatic controls on flood frequency requires understanding the modulation of the flood-generating mechanisms: for example, frontal systems, monsoonal flows, and tropical storms. In that sense, identifying the weather phenomena associated with the extremes is an important step in determining the physical mechanisms by which precipitation extremes are impacted by not only ENSO, but by a host of other short-term climate variations such as the PNA pattern, the North Atlantic Oscillation, and the Arctic Oscillation.

In this paper, we examine the impact of ENSO on extreme winter precipitation events over the United States. We characterize the spatial and temporal characteristics of the leading weather systems responsible for the precipitation extremes and quantify the impact of ENSO on the most extreme events. The results are presented for 49 winters (1949/50–1997/98) of daily precipitation observations and for an ensemble of nine simulations with an atmospheric general circulation model forced by observed sea surface temperatures covering the same time period. Section 2 describes the data and methodology. The results for the observations are presented in section 3 and the model results are presented in section 4. The discussion and conclusions are given in section 5.

2. Data and methodology

The observations consist of 49 winters (1949/50–1997/98) of daily continental U.S. gridded precipitation data (Higgins et al. 1996), and daily 500- and 300-mb height fields from the National Centers for Environmental Prediction–National Center for Atmospheric Research (NCEP–NCAR) reanalyses (Kalnay et al. 1996). All fields are put on a 2° latitude × 2.5° longitude grid to be consistent with the model results.

The model results are based on nine simulations with version 1 of the NASA Seasonal to Interannual Prediction Project (NSIPP-1) atmospheric general circulation model (AGCM) forced with observed SSTs for the same time period. The runs differ only in their initial atmospheric conditions: these were chosen arbitrarily from previously completed simulations. The NSIPP-1 AGCM is a gridpoint model. The dynamical core is described in Suarez and Takacs (1995). The boundary layer scheme is a simple K scheme, which calculates turbulent diffusivities for heat and momentum based on Monin–Obukhov similarity theory (Louis et al. 1982). The AGCM uses the relaxed Arakawa–Schubert (RAS) scheme to parameterize convection (Moorthi and Suarez 1992). The parameterization of solar and infrared radiative heating is described in Chou and Suarez (1994, 2000). The mosaic model (Koster and Suarez 1996) is used to represent land processes. Vegetation is prescribed with a climatological seasonal cycle. The simulations described here use a uniform horizontal resolution of 2° latitude × 2.5° longitude and 34 unequally spaced σ layers with high resolution (<200 m) in the lower 2 km of the atmosphere. Details of the NSIPP-1 model formulation and its climate are described in Bacmeister et al. (2000). The seasonal predictability of the model is described in Pegion et al. (2000) for boreal winter and in Schubert et al. (2002) for boreal summer.

We expand the daily winter [December–February (DJF)] precipitation fields in rotated (using varimax rotation) empirical orthogonal functions (EOFs). The daily anomalies were computed with respect to the 49-winter monthly climatology. Composites of precipitation and 500-mb height fields are developed based on the time history of the principal component (PC) of the precipitation EOF expansion. We do this by forming averages of these fields for all days during which the leading precipitation PC values have a local maximum that exceeds four standard deviations (this serves to

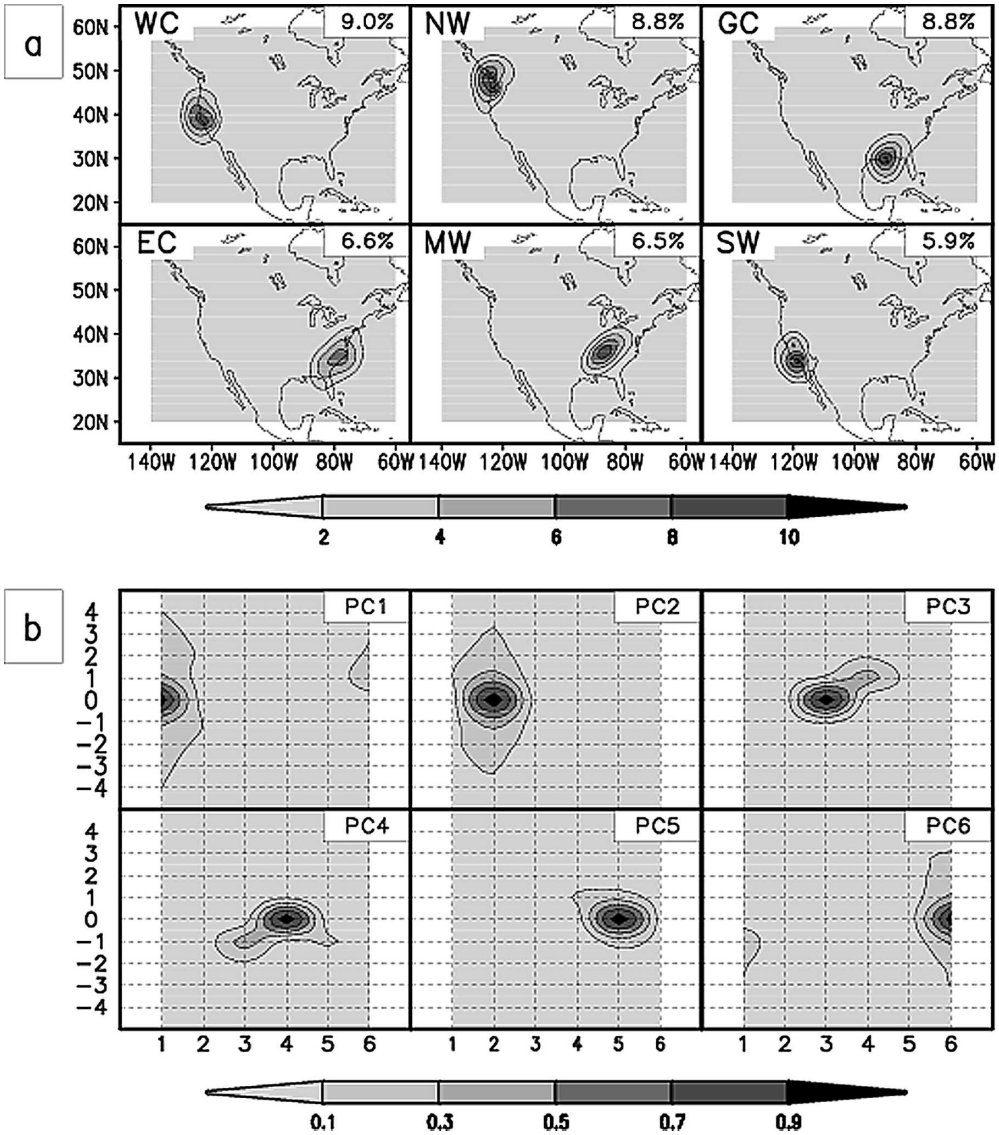

FIG. 1. (a) The six leading precipitation EOFs based on 49 winters (DJF 1949/50–1997/98) of daily NOAA precipitation observations. The numbers refer to the percent variance explained by each of the EOFs. The standard deviations of the six leading PC values are 0.93, 0.91, 0.87, 0.79, 0.77, and 0.75, respectively. Units are such that the PC values times the values in (a) have units of mm day^{-1}. The EOFs are referred to by their location (West Coast: WC, Northwest: NW, Gulf Coast: GC, East Coast: EC, Midwest: MW, and Southwest: SW). (b) The auto- and cross correlations of the six leading PCs. The ordinate shows the lag in days. The abscissa shows the PC number. For example, the top left panel shows the correlations between PC 1 and all the other PCs, the top middle panel shows the correlations between PC 2 and all other PCs, etc.

define day 0). Additional composite fields are produced at various time lags (± 1, ± 2 days) with respect to day 0 to obtain a sense of the evolution of the patterns. We note that this EOF-based approach implicitly assumes that any impact of ENSO on the weather extremes is primarily manifest as changes in the temporal behavior of the weather systems. Since the EOF patterns are fixed, the approach does not allow for any changes in spatial structure of the weather systems. While we do not rule out that possibility, it is likely that any such changes would be difficult to detect and verify given the relatively small sample size provided by the observations.

Various aspects of the extreme-value analysis are described as the topics are introduced in subsequent sections.

3. Analysis of the observations

We begin by analyzing the observations. We present in section 3a the characteristics of the leading precipitation EOFs and in section 3b various composites based on the extreme values of the associated PCs. This is followed in section 3c by a statistical analysis of the winter maxima.

a. The leading precipitation EOFs

The six leading rotated EOFs of the continental U.S. daily precipitation data are shown in Fig. 1a. The patterns are to a large extent localized (a feature emphasized by rotation) and emphasize variability on both the West and East Coasts. EOFs 1, 2, and 6 characterize precipitation variability on the West Coast: for future reference these EOFs are denoted as the West Coast (WC) EOF, the Northwest (NW) EOF, and the Southwest (SW) EOF, respectively. Furthermore, EOF 3 is denoted as the Gulf Coast (GC) EOF, EOF 4 is the East Coast (EC) EOF, and EOF 5 is the Midwest (MW) EOF. This naming convention and our subsequent association of these EOFs with specific storm systems is based on the following composite analysis. While there is no clear cutoff or drop in the variance associated with the higher-order EOFs, we do find that the EOF patterns and associated time series become increasingly less coherent. Figure 2 shows that the six leading EOFs account for a major fraction (>50%) of the daily precipitation variance over much of the West Coast and southeastern part of the country.

We show in Fig. 1b the autocorrelations and the cross correlations between the six leading PCs. The autocorrelations show a rather interesting difference between the West and East Coast, with the West Coast PCs showing a local time scale of 4–8 days, while the eastern PCs typically have a local time scale of about 2 days. We note that, while this does not necessarily reflect the lifetime of the associated storm system (we shall see next that they propagate), it is an important indicator of the amount of precipitation that will fall in any one location associated with these storms. The cross correlations tend to be weak with values generally less than 0.3. The largest cross correlations are between PCs 3 and 4 at a lag of 1 day (values range between 0.3 and 0.4), suggesting that these EOFs tend to be associated with the same storm system. In fact, we shall see next that these patterns represent somewhat different origins and/or tracks of well-known storm systems.

The composite fields (precipitation and 500-mb heights) associated with six leading EOFs are shown in Fig. 3. For the WC EOF (first column in Fig. 3), the composite 500-mb height anomalies initially (day −2) have a northwest–southeast orientation with a positive anomaly over Alaska and a negative anomaly off the coast of California. The system moves slowly onto the West Coast with the leading edge of the negative anomaly impinging on California at day 0. The system remains largely stationary, though it develops a more zonal orientation after day 0 as energy propagates toward the east and the system weakens. An inspection of the WC PC time series shows that the largest amplitude events are associated with major flooding episodes on the West Coast (especially California). A peak in the PC in December 1955 is, for example, associated with what was called the "Big Flood" and was deemed by the California Disaster Office to be "the greatest disaster of its kind which ever occurred in California" (additional information is available online at http://www.siskiyous.edu/shasta/env/storm).

The NW EOF composite 500-mb height anomalies show at day −2 a negative anomaly over British Co-

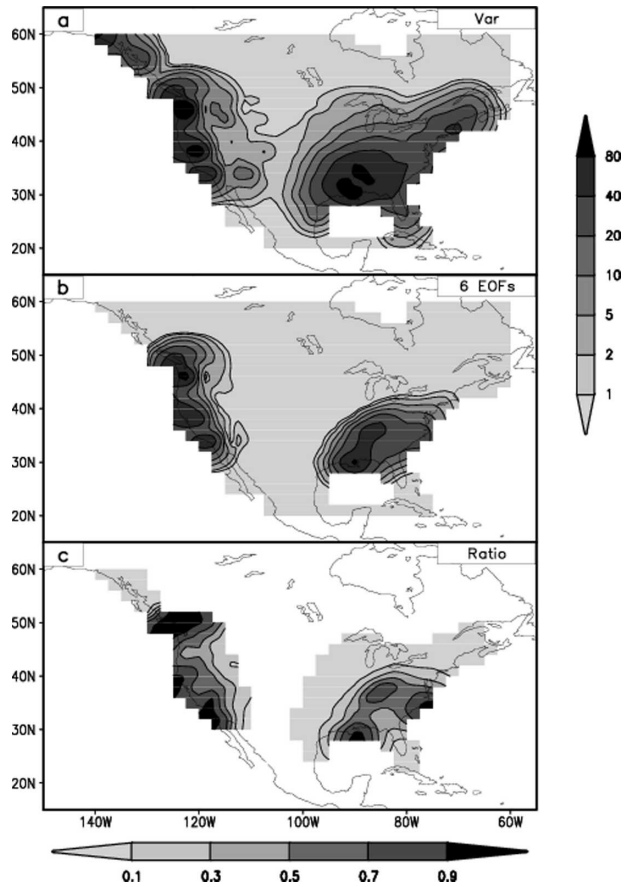

FIG. 2. (a) The variance of daily precipitation (DJF 1949/50–1997/98). (b) The contribution to the variance from the six leading PCs. (c) The ratio of the variance associated with the six leading PCs to the total variance (b/a). Units of variance are (mm day^{-1})^2.

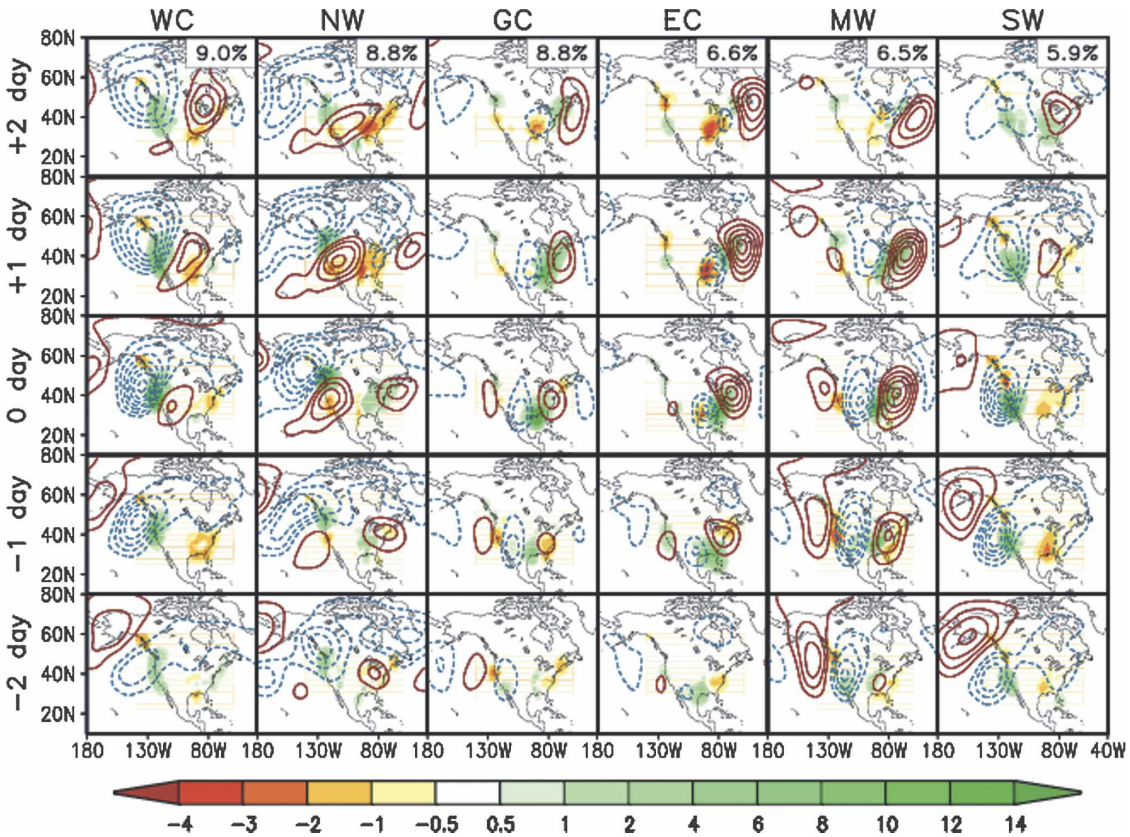

FIG. 3. Composite maps associated with the six leading rotated EOFs of the daily precipitation for DJF 1949/50–1997/98. The precipitation anomalies are shaded (mm day^{-1}), and the contours are the 500-mb height anomalies (contour interval is 25 m). The composite at day 0 includes all times when the associated PC exceeds four standard deviations.

lumbia that retrogrades, moving over the Gulf of Alaska by day 0 during which it produces the greatest precipitation over the northwest coast. A positive anomaly develops to the southwest such that by day +1 it covers much of the western United States. The negative anomaly moves northward and westward over northwestern Canada and Alaska as it weakens. An inspection of the PC time series shows that large values of this PC are also associated with flooding on the West Coast, though in this case the flooding tends to occur farther to the north. For example, this EOF appears to be associated with an unusually intense and long lasting storm that occurred in the Pacific Northwest during 5–9 February 1996. The EOF also appears to have played an important role in the West Coast flooding during December and first week of January 1996/97.

The precipitation maximum for the SW EOF (sixth column in Fig. 3) occurs somewhat farther south (primarily over southern California) compared with the other two West Coast EOFs. The associated 500-mb height anomalies are similar to those for the WC EOF, though the anomalies are considerably stronger at day −2, and the negative anomaly tends to take on a zonal orientation earlier in its development (day 0 and earlier) compared with the strong northwest–southeast orientation of the WC EOF during that phase. An inspection of PC time series shows again that large values of this PC are associated with flooding on the West Coast, though in this case the flooding tends to occur farther to the south. This PC also tends to be more episodic compared with the other two, with strong events followed by long periods of no activity. The SW EOF is associated with the major floods in southern California during January–February 1969 (twin floods of 1969 at Huntington Beach) and January–February 1980. This EOF was also active during recent El Niño winters. For example, the 1997/98 winter was one of the wettest on record across California. The periods 29 December 1992 and 5–19 January 1993 were also very wet.

The GC EOF (third column in Fig. 3) is associated with a storm system that apparently enters the southern United States as a weak system from the Pacific (day −2), and strengthens as it crosses the southern tier of states and the Gulf of Mexico: the western Gulf of Mexico is

an area that is known to be a preferred region of cyclogenesis (Whittaker and Horn 1984). Large precipitation amounts occur initially in the Gulf States (day 0) as the system taps moisture from the Gulf of Mexico. This is followed by widespread precipitation that covers much of the eastern United States as the system moves to the northeast (day +1). Some of the strongest storms associated with this EOF occurred during the 1977/78, 1978/79, and the 1997/98 winters.

The composite evolution of the EC EOF (fourth column in Fig. 3) shows that the storm apparently develops over the northwest Gulf of Mexico/Texas (day −2) and propagates to the northeast. At day 0 the system is associated with precipitation over much of the Atlantic seaboard. At day +1 the system is generating precipitation largely over the northeastern states and is dominated by a strong positive height anomaly centered over Nova Scotia. As mentioned earlier, the EC PC has a substantial correlation with the GC PC at a lag of 1 day in the sense that the EC PC tends to follow the GC PC by one day. This connection is consistent with the life cycle of some nor'easters that initially track from the western Gulf of Mexico to the east-northeast and then redevelop off the East Coast and propagate to the north. An inspection of the PC time series suggests that there are also a number of events described by just one or the other of the EOFs alone (e.g., a peak in GC PC during 1978/79 and the peak in EC PC during 1957/58). The EC PC appears to be associated with several major blizzards along the East Coast including the Blizzard of 1966 (29–31 January), the 5–7 February 1967 storm, the 10–12 February 1983 Presidents' Day storm, the two January 1987 storms (21–23 and 25–27), and several East Coast storms during the winter of 1997/98. Somewhat surprisingly, some of the other major nor'easters of the twentieth century (e.g., the Lindsay storm of 8–10 February 1969 and the 18–19 February 1979 Presidents' Day snowstorms) do not show up very prominently in the leading PC time series. It is likely that this occurs because our methodology is focused on precipitation maxima, so major snow producing storms that tend to have less precipitation than the warmer storms are underrepresented.

The composite fields of the MW PC (fifth column in Fig. 3) show that it is associated with a storm system that enters the United States from the Gulf of Alaska, tracking across the midcontinent where it produces precipitation in the Southwest (day −1) and eventually (day +1) produces precipitation covering much of the eastern United States. The most intense precipitation associated with this storm at day 0 occurs over a wide swath extending from Louisiana to Pennsylvania. An inspection of the time series of the PC shows that this EOF was apparently quite active during the 1950s and rather inactive during much of the 1980s. As an example, this EOF was particularly active during the winter of 1949/50 in which it was associated with three separate storms. More recently, this EOF was associated with major winter storms in early December 1978 that affected much of the Midwest and eastern United States.

b. The link to ENSO

In this section we examine the seasonal mean conditions that favor the leading EOF patterns. Likewise, we would like to determine the mean conditions that are associated with depressed activity in these weather patterns. We begin by developing a simple measure of the activity of the EOF patterns. The activity for winter i is defined as

$$\sigma_i^2 = \frac{1}{L}\sum_{k=1}^{L} z_{ik}^2, \tag{1}$$

where the sum is over the L days of winter (DJF), and the z_{ik} are the PCs at day k of winter i.

Table 1 orders the 49 winters according to the activity associated with each of the six leading EOFs. It is evident that there is a predilection for enhanced activity in the GC, EC, and SW EOFs during El Niño winters, while the GC storm also tends to be suppressed during cold (La Niña) years. The results for the SW EOF are generally consistent with previous studies of ENSO and precipitation over California (e.g., Yarnal and Diaz 1986; Schonher and Nicholson 1989; Mo and Higgins 1998; Cayan et al. 1999; Higgins et al. 2000). The other EOFS do not show a clear impact from ENSO, though there is an overall tendency (across all the leading EOFs) for the years with weak activity to be associated with La Niña winters, while the years with strong activity tend to be associated with El Niño winters.

Figures 4 and 5 show the average of the 300-mb height and SST anomalies for the 10 winters with the strongest (referred to as active winters) and weakest (referred to as quiet winters) activity (Table 1) in the GC, EC, and SW PCs. Here the anomalies are computed with respect to the average of the 29 remaining years that have moderate activity in each EOF. We note that, while the SST composites for the WC, NW, and MW EOFs (not shown) do not show a clear impact from ENSO, there is a tendency for these EOFs to be associated with a trough (ridge) off the West Coast during active (quiet) years.

The average 300-mb height anomalies associated with the strongest activity in the GC and EC PCs (left panels of Fig. 4) are similar, with both suggesting a link to El Niño (e.g., Hoerling and Kumar 1997). The

TABLE 1. List of the winters (DJF) ordered by increasing activity for each of the leading PCs. See text for definitions. Blue indicates La Niña years, and red indicates El Niño years. Bold indicates major events. Italics indicate weak events. The classification of the years into warm and cold events is that of the Climate Prediction Center for January through March of each year (the classification scheme is subjective and is based on SST analyses).

WC	NW	GC	EC	MW	SW
76–77	*54–55*	**88–89**	**88–89**	85–86	63–64
75–76	51–52	70–71	*49–50*	76–77	*50–51*
88–89	76–77	93–94	*79–80*	*95–96*	*64–65*
63–64	*92–93*	*74–75*	85–86	80–81	67–68
90–91	*84–85*	*75–76*	*87–88*	**97–98**	60–61
71–72	**57–58**	59–60	*50–51*	62–63	86–87
54–55	61–62	61–62	56–57	*79–80*	52–53
84–85	63–64	*50–51*	*55–56*	*84–85*	**88–89**
91–92	65–66	*49–50*	68–69	*77–78*	*69–70*
56–57	**88–89**	67–68	80–81	59–60	76–77
93–94	78–79	62–63	51–52	96–97	*54–55*
89–90	62–63	56–57	*64–65*	67–68	*49–50*
70–71	86–87	85–86	*95–69*	63–64	80–81
86–87	*58–59*	**73–74**	61–62	*92–93*	89–90
87–88	*55–56*	*84–85*	70–71	*83–84*	70–71
65–66	**97–98**	94–95	75–76	68–69	65–66
73–74	68–69	*69–70*	52–53	75–76	93–94
60–61	*69–70*	68–69	62–63	60–61	56–57
74–75	93–94	*55–56*	76–77	**57–58**	81–82
49–50	*83–84*	*83–84*	96–97	**82–83**	59–60
59–60	*74–75*	52–53	53–54	71–72	71–72
61–62	*64–65*	89–90	93–94	65–66	*87–88*
67–68	*49–50*	*95–96*	60–61	*58–59*	*84–85*
72–73	59–60	60–61	67–68	86–87	96–97
53–54	52–53	96–97	71–72	52–53	*58–59*
58–59	96–97	66–67	*69–70*	*64–65*	62–63
79–80	56–57	*79–80*	*84–85*	81–82	75–76
94–95	**91–92**	72–73	*74–75*	94–95	*95–96*
57–58	*77–78*	71–72	**91–92**	*74–75*	72–73
78–79	*87–88*	80–81	*58–59*	70–71	*55–56*
83–84	66–67	51–52	*54–55*	*55–56*	*83–84*
62–63	72–73	**57–58**	*83–84*	66–67	**73–74**
80–81	80–81	81–82	89–90	72–73	53–54
50–51	60–61	63–64	72–73	89–90	78–79
66–67	*50–51*	*87–88*	*77–78*	*87–88*	61–62
51–52	*90–91*	53–54	*90–91*	*54–55*	*74–75*
52–53	53–54	*64–65*	66–67	53–54	85–86
64–65	*95–96*	*58–59*	**73–74**	*50–51*	*90–91*
77–78	70–71	76–77	**57–58**	56–57	**91–92**
96–97	85–86	*92–93*	65–66	**73–74**	**82–83**
92–93	**73–74**	86–87	81–82	51–52	**57–58**
85–86	71–72	*54–55*	94–95	*69–70*	51–52
68–69	67–68	65–66	*92–93*	**88–89**	66–67
69–70	*75–76*	*77–78*	63–64	**91–92**	*77–78*
81–82	89–90	78–79	86–87	93–94	94–95
97–98	*79–80*	**91–92**	59–60	61–62	*79–80*
82–83	94–95	*90–91*	78–79	*49–50*	**97–98**
55–56	**82–83**	**82–83**	**82–83**	78–79	68–69
95–96	81–82	**97–98**	**97–98**	*90–91*	*92–93*

anomalies consist of enhanced heights in the Tropics, a negative anomaly in the far-eastern North Pacific extending into the southwestern United States, and a positive anomaly over much of Canada. The anomalies are somewhat stronger for the EC PC. The link to ENSO is supported by the SST anomalies (right panels of Fig. 4), which show El Niño–like positive anomalies in the eastern tropical Pacific for the active years of both PCs.

The composites for the quiet years for the two PCs are quite different. The composite for the GC PC shows a link to La Niña (reduced tropical heights and a positive anomaly in the eastern North Pacific), while the composite for the EC PC shows a weak wave train extending from the Aleutian Islands into the United States where a positive anomaly extends from the Gulf of California to the Great Lakes. The link to La Niña for the GC PC is supported by the composite cold SST anomalies in the eastern tropical Pacific during the inactive years. On the other hand, the composite SST anomalies for the EC PC quiet years show very few if any significant SST anomalies.

The average conditions associated with the strongest activity in the SW PC (top left panel of Fig. 5) shows perhaps the strongest link with El Niño, with a well-defined wave train in the eastern Pacific and over North America. These anomalies produce an eastward extension and enhancement of the Pacific trough that presumably fosters the growth of the West Coast weather systems. The strong link with El Niño is supported by the SST anomalies (top right panel of Fig. 5). During the quiet winters (middle left panel of Fig. 5), the Pacific Northwest and much of Canada is dominated by an anomalous ridge, while an anomalous negative height anomaly is situated near the date line in the North Pacific. The height anomalies in this case are not simply the negative of the mean anomaly pattern for the active years and are situated farther west over the North Pacific than what one might expect from a La Niña response. The SST anomalies (middle right panel of Fig. 5), in fact, show few significant anomalies other than those over the North Pacific, and these are likely a response to the atmospheric anomalies.

c. *Extreme value analysis*

In this section we examine the statistics of the PCs associated with the upper tails of the governing probability density functions (PDFs) and how they depend on ENSO. Specifically we look at how ENSO impacts the winter maxima. In view of our short data record, we have attempted to reduce the sampling errors in our estimates by taking a parametric approach to estimating the relevant statistics. In particular, we fit the

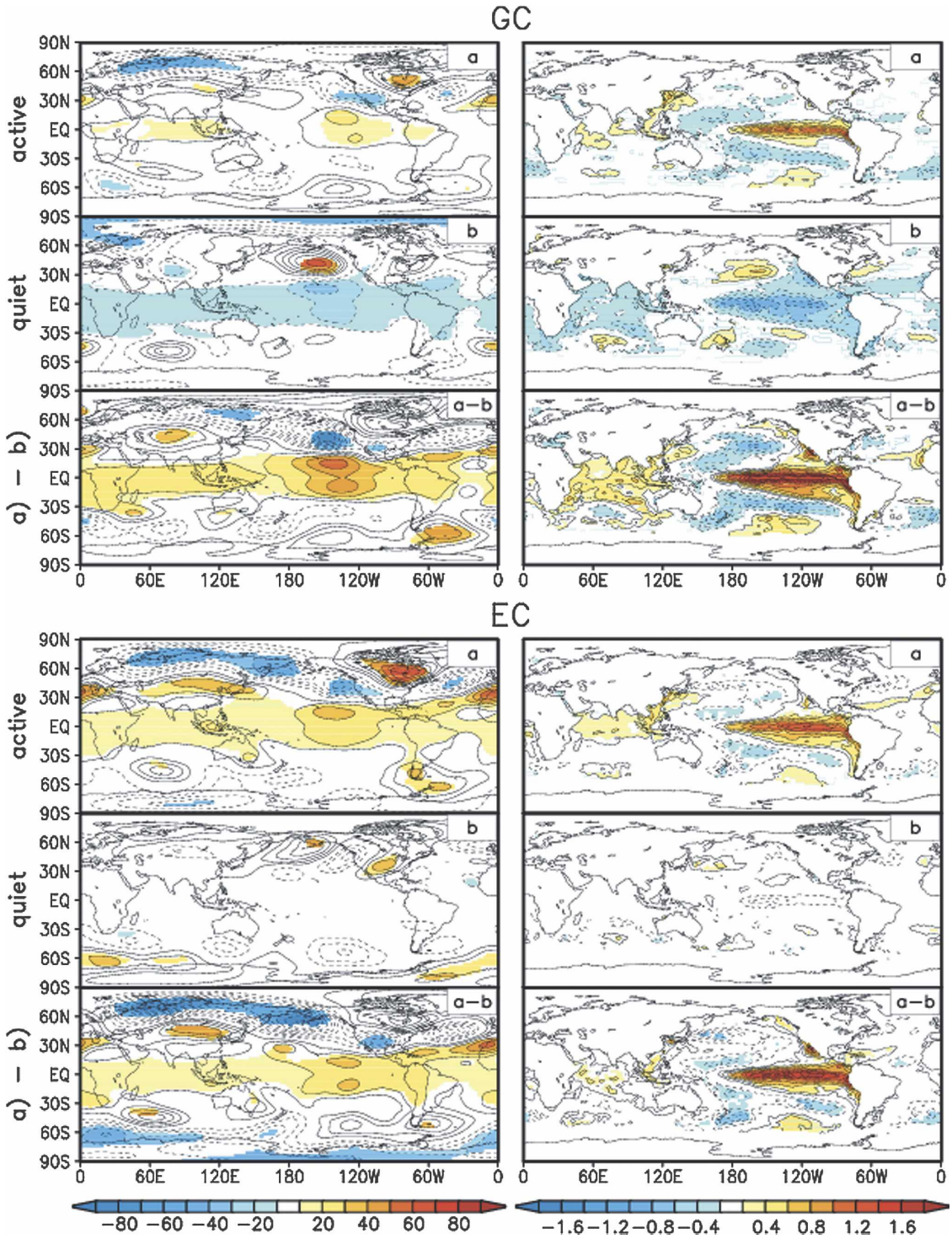

FIG. 4. Composite anomaly maps of the seasonal mean (DJF) 300-mb heights (left panels) and SST anomalies (right panels) averaged over the 10 winters with the largest (least) PC activity (the years are listed in Table 1). For each set of panels, the third panel shows the difference fields. The anomalies are computed with respect to the mean of the 29 remaining years. The top panels are for PC 3 (GC) and the bottom panels are for PC 4 (EC). Units are in meters. Shading indicates significance at the 10% level based on a *t* test.

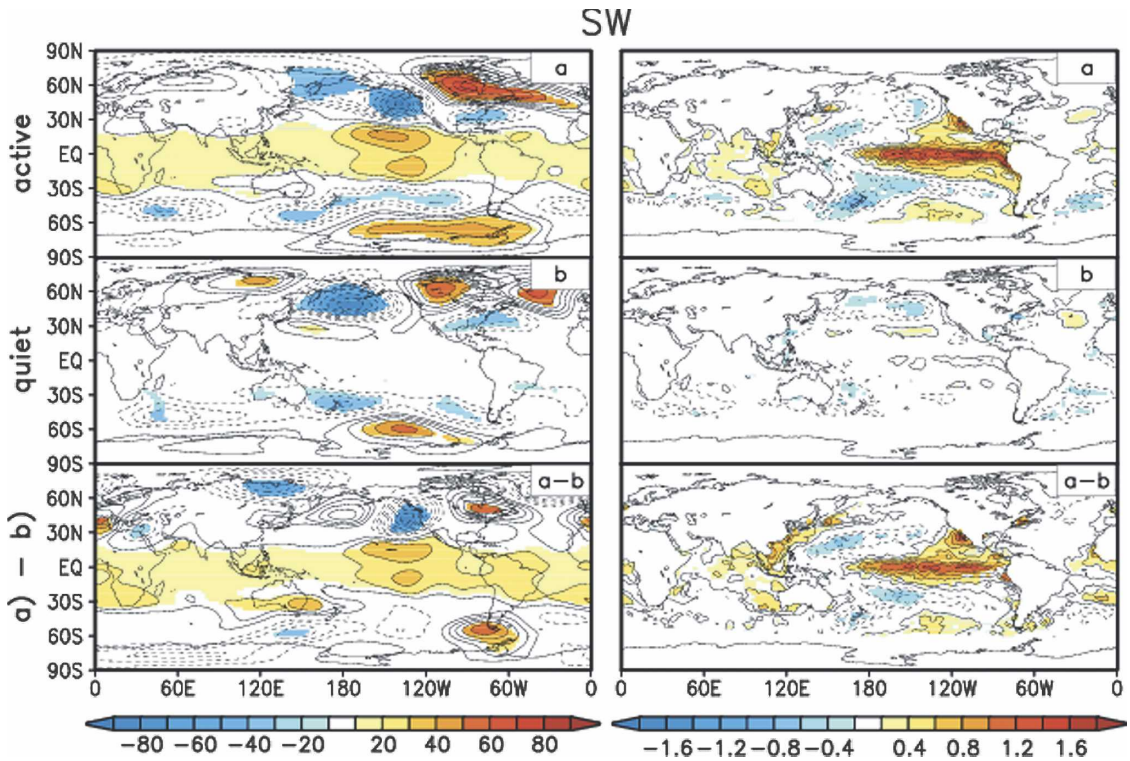

FIG. 5. As in Fig. 4, except for PC 6 (SW).

maxima (one for each winter) to a class of extreme value (EV) distributions. All subsequent statistical analysis was carried out using either the "XTREMES" software package (Reiss and Thomas 1997), or the "extremes" software (additional information is available online at http://www.assessment.ucar.edu/toolkit/index.html).

Our focus here is on the statistics of the largest values. The PDFs of the winter maxima are estimated by fitting extreme value distributions to the winter (DJF) daily maximum values for the period December 1949 through February 1998. In particular, we fit the maximum values to the "generalized extreme value" (GEV) cumulative distribution function (Coles 2001):

$$G(x) = \exp\left\{-\left[1 + \zeta\left(\frac{(x-\mu)}{\sigma}\right)\right]^{-1/\zeta}\right\}, \qquad (2a)$$

with location parameter (μ), scale parameter (σ), and shape parameter (ζ). Here $\{x: 1 + \zeta(x - \mu)/\sigma > 0\}$, $-\infty < \mu, \zeta < \infty$ and $\sigma > 0$. The Gumbel distribution is a special case of the GEV where ($\zeta = 0$) such that

$$G_o(x) = \exp\left\{-\exp\left[-\left(\frac{x-\mu}{\sigma}\right)\right]\right\}. \qquad (2b)$$

The shape parameter of the GEV distribution governs the tails of the distribution, while the location parameter is related to the mean (it is equal to the mode in the Gumbel distribution), and the scale parameter is related to the variance. We note that the Gumbel distribution is actually one of three submodels of the GEV distribution, the other two being the Frèchet ($\zeta > 0$) and reverse Weibull ($\zeta < 0$). The N-year return value for the GEV distribution (the value that is on average exceeded once in N years) is

$$X_N = \mu - \frac{\sigma}{\zeta}\left\{1 - \left[-\ln\left(1 - \frac{1}{N}\right)\right]^{-\zeta}\right\}, \qquad (3a)$$

and for the Gumbel distribution it is

$$X_{oN} = \mu - \sigma \ln\left[-\ln\left(1 - \frac{1}{N}\right)\right]. \qquad (3b)$$

We found that, for the observations, the Gumbel distribution provides a reasonable representation of the distribution of the maximum values of the PCs. It is however likely that the limited sample size (49 winters) is simply insufficient to allow estimating a statistically significant shape parameter (see section 4). Table 2a shows the parameters (location and scale) of the fits to the Gumbel PDF for the six leading PCs including the 90% confidence intervals (CIs). The CIs are estimating using a Monte Carlo bootstrap approach (Reiss and Thomas 1997) in which we generate 2000 synthetic

TABLE 2a. The parameter estimates (columns 2 and 3) of the fitted Gumbel distributions for the six leading PCs. Values are based on the maximum values for all winters (DJF) for the period 1949–98. Values in parentheses are the 90% confidence intervals based on Monte Carlo simulations. The fourth column shows the 20-yr return values in units of standard deviation.

PC	μ	σ	X_{20}
1 (WC)	3.60 (3.31, 3.93)	1.24 (1.00, 1.45)	7.9
2 (NW)	3.19 (3.01, 3.39)	0.79 (0.63, 0.92)	6.0
3 (GC)	3.80 (3.46, 4.16)	1.38 (1.10, 1.62)	9.1
4 (EC)	3.21 (2.97, 3.46)	0.99 (0.79, 1.15)	7.7
5 (MW)	2.97 (2.74, 3.23)	0.98 (0.79, 1.15)	7.7
6 (SW)	3.09 (2.77, 3.42)	1.32 (1.07, 1.54)	9.4

samples of 49 extreme values with the fitted Gumbel distribution in order to generate the sampling statistics of the parameters. The 20-yr return values range from six standard deviations for the NW storms to more than nine standard deviations for the GC and SW storms. This highlights the intensity of the extreme GC and SW storms as measured in terms of their typical daily variability.

In view of the fact that some of the PCs are influenced by ENSO, the above return values are somewhat misleading since decades dominated by El Niño events would presumably have EV statistics that are different from those with decades that have primarily La Niña or neutral conditions. To address this dependence, we repeat the extreme value analysis but carry out separate fits to the data for the La Niña, neutral, and El Niño years.[1] Following Katz et al. (2002), we make use of an effective return period N^*, defined for the GEV distribution as

$$N^* \equiv \left\{1 - \exp\left[-\left(1 + \zeta^* \frac{X_N - \mu^*}{\sigma^*}\right)^{-(1/\zeta)}\right]\right\}^{-1}, \quad (4a)$$

and for the Gumbel distribution as

$$N^* \equiv \left\{1 - \exp\left(-\exp\left[\frac{X_N - \mu^*}{\sigma^*}\right]\right)\right\}^{-1}, \quad (4b)$$

where the asterisk indicates conditional parameter values, and X_N is the unconditional N-year return value For example, one might compute X_N from a full record and then recalculate the parameters only for El Niño years. In that way the impact of El Niño can be more readily quantified in terms of the change in the return period (e.g., the N = 20-yr unconditional return value might become an N^* = 5 yr return value when conditioned on El Niño).

[1] We also carried out an analysis in which the impact of ENSO was modeled as a covariate in the fit to the Gumbel distribution by assuming a linear dependence of the parameters on ENSO following Katz et al. (2002). The results were generally (with the exception of the SW storm) very similar to those shown in Table 2b. The nonlinearity (asymmetry) of the SW storm response to ENSO, however, made this linear approach less attractive.

TABLE 2b. The parameter estimates of the Gumbel distribution for the leading PCs impacted by ENSO. Separate fits are done for El Niño (15), La Niña (13), and neutral (20) winters (DJF) for the period 1949–98. The scale parameter (σ) is fixed in advance at the estimates obtained from the full record (Table 2a). Values in parentheses are the 90% confidence intervals in the location parameter (μ). The last column shows the effective return period (in years) that the X_{20} value (obtained from the entire record) would have under warm, cold, or neutral ENSO conditions. See text for details.

PC	ENSO	μ	σ fixed	N^*
3 (GC)	Warm	4.58 (4.1, 5.3)	1.38	11.6
	Cold	3.23 (2.7, 4.0)	1.38	30.0
	Neutral	3.74 (3.3, 4.3)	1.38	20.9
4 (EC)	Warm	3.77 (3.4, 4.2)	0.99	11.0
	Cold	2.76 (2.4, 3.3)	0.99	29.7
	Neutral	3.23 (2.9, 3.6)	0.99	18.7
6 (SW)	Warm	3.84 (3.3, 4.5)	1.32	11.5
	Cold	2.83 (2.3, 3.5)	1.32	24.1
	Neutral	2.82 (2.3, 3.3)	1.32	24.2

The results of fitting the Gumbel distribution separately to El Niño, La Niña, and neutral years shows that only the location parameter is impacted by ENSO—there are no significant impacts from ENSO on the scale parameter. In fact, we take advantage of this result by fixing the scale parameter to be that estimated from the full record (Table 2a), thereby reducing the number of free parameters in the final fit. Table 2b shows the results for those PCs that are significantly impacted by ENSO. Both the GC and EC storms have significantly different location parameters during cold and warm years. The SW storms, in contrast, are significantly impacted by El Niño, but the results for La Niña years are indistinguishable from those for neutral years. The impact is quantified in the last column in Table 2b in terms of the impact on the return values. The results are such that extreme GC, EC, and SW storms that occur on average only once every 20 years (20-yr storms) would occur on average in half that time under El Niño conditions. In contrast, under La Niña conditions, 20-yr GC and EC storms would occur on average about once in 30 years, while there is little impact of La Niña on the intensity of the SW storms

4. Analysis of the model simulations

We next repeat the analysis of the previous section using the output from the NSIPP-1 model simulations. As described previously, the runs consist of nine en-

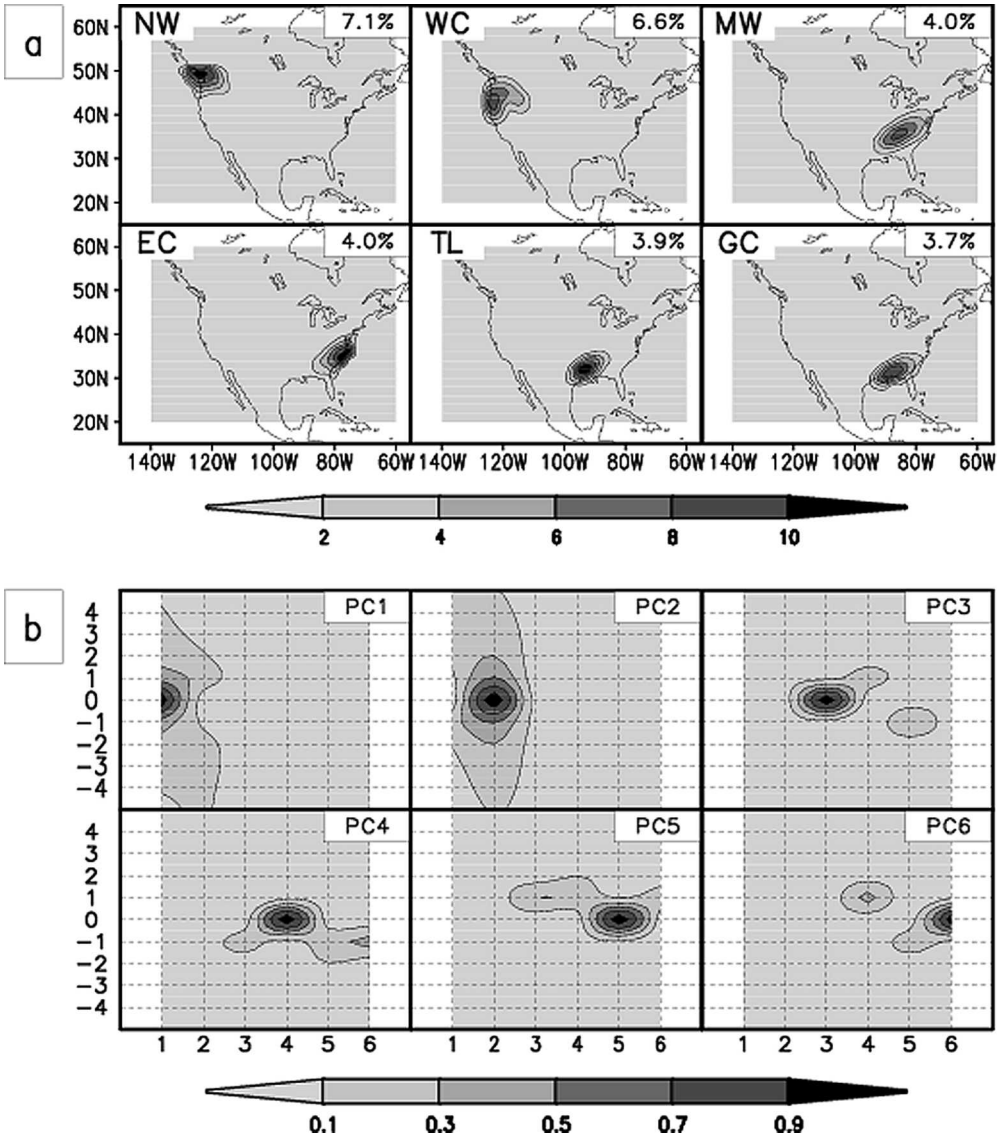

FIG. 6. As in Fig. 1, except for the results based on an ensemble of nine NSIPP-1 AGCM simulations with observed SSTs. The standard deviations of the six leading PC values are 0.70, 0.68, 0.53, 0.53, 0.52, and 0.51, respectively. The EOFs are referred to by their locations.

semble members forced with observed SSTs over the same time period that was analyzed for the observations (1949–98). We again begin by presenting the characteristics of the leading simulated precipitation EOFs and various composites based on the extreme values of the associated PCs. This is followed by the statistical analysis of the winter maxima. Since we have a sample size that is 9 times larger than that of the observations, we should be able to provide a better assessment of the quality of the fits to the various extreme value distributions than was possible for the observations.

We note that an alternative approach to analyzing the AGCM results is to project the model fields onto the EOFs computed from the observations. We found that, while the model does produce very realistic precipitation EOFs (see below), relatively small shifts in the location of the simulation EOF (compared with the analogous EOF from the observations) can produce rather unrealistic results when projecting the model fields onto the observationally based EOFs. As a result, we did not pursue that approach here.

a. The leading simulated precipitation EOFs

The six leading rotated EOFs of the simulated continental U.S. daily precipitation data are shown in

Fig. 6a. The patterns are to a large extent quite similar to those based on the observed fields, emphasizing the variability on the West Coast and the southeast. One overall difference to note is that the leading model EOFs tend to have less variance than the observed (roughly only about one-half the variance). This is likely strongly impacted by the relatively coarse (2° latitude × 2.5° longitude) resolution of the model simulations. Nevertheless, most of the six leading EOFs can be associated with one of the leading observed patterns (cf. Fig. 1a). In particular, EOF 1 is similar to the NW EOF, EOF 2 is similar to the WC EOF, EOF 3 is similar to the MW EOF, EOF 4 is similar to the EC EOF, and EOF 6 is similar to the GC EOF. Only the fifth EOF, situated over Texas/Louisiana does not have a companion in the observations. We will refer to this EOF as the TL EOF. Also, the SW EOF does not appear to have a companion in the simulation. This is indicative of an overall insufficient amount of precipitation variance over southern California and surrounding regions compared with the observations (cf. Figs. 2a and 7a). While the nature of this model deficiency is unclear, there is evidence that the MJO plays an important role in the development of some of the major winter storms that affect this region (e.g., Bell and Higgins 2005). Since the model has only a very weak MJO, it would not be surprising that the model does not produce these major winter storms. Figure 7c shows that the six leading EOFs account for a realistic fraction (>50%) of the simulated daily precipitation variance over much of the West Coast (with the exception noted above) and southeastern part of the country.

Figure 6b shows the autocorrelations and the cross correlations between the six leading simulated PCs. The autocorrelations show the same difference between the West and East Coast that we saw in the observations, with the West Coast PCs showing a longer local time scale (in this case even longer—up to 10 days), while the eastern PCs typically have a local time scale of about 2 days. The cross correlations again tend to be weak with values generally less than 0.3. The largest cross correlations (values range between 0.3 and 0.4) are between PCs 4 (EC) and 6 (GC) at a lag of 1 day, suggesting that these EOFs tend to be associated with the same storm system—similar to what was found for the observations for the EC and GC storms. We also see a connection between PC 5 (TL) and PC 3 (MW), suggesting that these two PCs at times represent the same storm system as it moves from Texas in a northeast direction.

The composite precipitation and 500-mb heights fields associated with the six leading EOFs are shown in

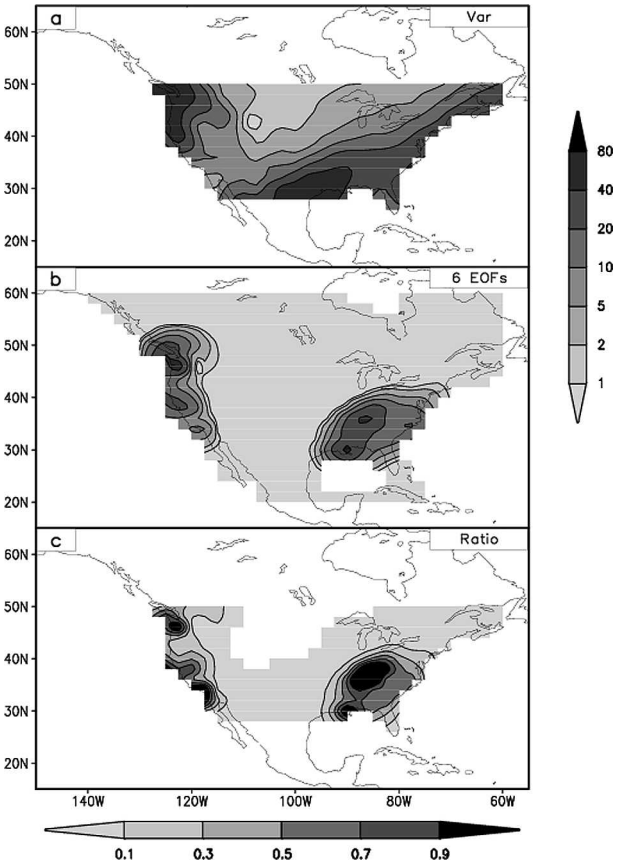

FIG. 7. (a) As in Fig. 2 except for the results based on an ensemble of nine NSIPP-1 AGCM simulations forced with observed SST.

Fig. 8. The basic features of these fields (the larger and longer time scales of the West Coast versus eastern U.S. storms) are reproduced in the model simulations. The overall development and orientation (northwest–southeast) of the West Coast storms (NW and WC) is also well captured by the model. The observed differences between the GC and EC storms is evident in the simulated EOFs as well, with the latter showing a southwest–northeast development along the East Coast, while the former tends to propagate across the southern tier of states and then move eastward into the Atlantic. The early development of the GC storm (days −1 and −2) is, however, quite different, with the model showing a somewhat larger-scale development that has a northwest–southeast structure and the observations showing a more zonal and smaller-scale structure. The evolution of the TL storm tends to occur just upstream and in quadrature with the MW storm, consistent with the cross correlations (Fig. 6b) that indicate these two EOFs emphasize different phases of the same storm.

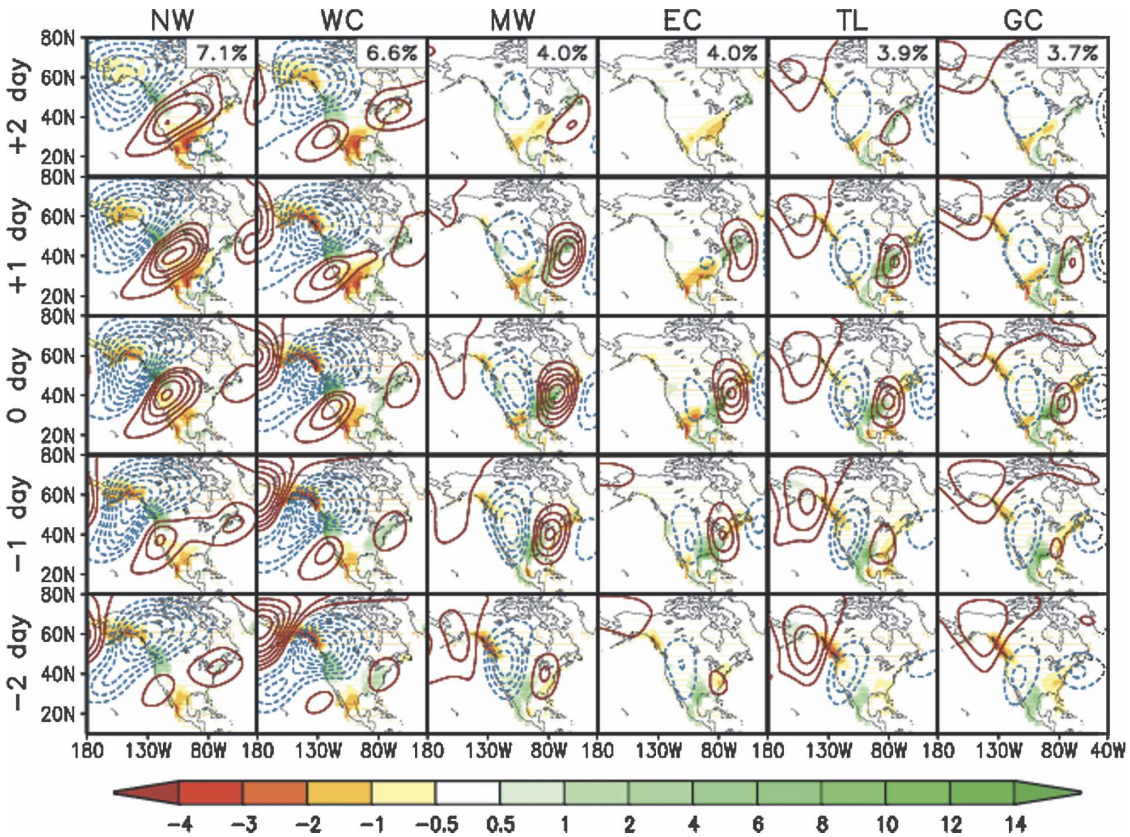

FIG. 8. As in Fig. 3, except for the six leading rotated EOFs from the model simulation.

b. *The link to ENSO*

In this section we examine the seasonal mean conditions that favor or depress the activity in the leading EOF patterns of the simulations. The measure of activity is defined in section 3b. Table 3 orders the 49 winters according to the activity associated with each of the six leading EOFs. There is a clear predilection for enhanced activity in the GC, EC, and TL EOFs during El Niño winters, while these storms tend to be suppressed during cold (La Niña) years. The other EOFS do not show a consistent impact from ENSO. Comparing with the observations (Table 1), we see a very similar impact of ENSO on the GC and EC storms. One difference is that the observed EC storm tends to be less clearly suppressed during cold events than is the case for the simulations (the years with suppressed activity include both cold and warm events).

We next focus on the EC and GC storms—the two storms that are clearly impacted by ENSO and that have counterparts in the observations. Figure 9 shows the average of the 300-mb height and SST anomalies for the 10 winters with the strongest and weakest activity (Table 3) in the GC and EC PCs. Both fields are quite similar for the two EOFs, reflecting the fact that the years included in the composites are essentially the same (there are only two years that are different in each composite). The anomalies consist of enhanced heights in the Tropics, a negative anomaly in the far eastern North Pacific extending into the southwestern United States, and a positive anomaly over much of Canada. The link to ENSO is supported by the SST anomalies (right panels of Fig. 9), which show El Niño–like positive anomalies in the eastern tropical Pacific for the active years of both PCs. The composites for the quiet years for the two PCs are also quite similar, which reduced tropical heights, and a positive anomaly in the eastern North Pacific, reminiscent of the response to La Niña SST anomalies (middle panels on the right side of Fig. 9).

c. *Extreme value analysis*

In this section we examine the statistics of the simulated storms (PCs). We again look at how ENSO impacts the winter maxima. Since we now have substantially more data points than we had for the observations (nine ensemble members), we are able to do a more refined fit to the EV distributions.

We begin by fitting the maximum values to the GEV

TABLE 3. As in Table 1, except for the model PCs.

NW	WC	MW	EC	TL	GC
64–65	**82–83**	59–60	49–50	59–60	**88–89**
55–56	79–80	68–69	59–60	49–50	75–76
73–74	86–87	75–76	50–51	50–51	70–71
58–59	95–96	87–88	**88–89**	**88–89**	**73–74**
77–78	51–52	49–50	75–76	75–76	49–50
95–96	80–81	94–95	95–96	63–64	59–60
80–81	**57–58**	53–54	**73–74**	79–80	53–54
50–51	83–84	95–96	60–61	74–75	60–61
93–94	**73–74**	51–52	52–53	66–67	50–51
78–79	65–66	**73–74**	70–71	52–53	96–97
81–82	77–78	52–53	55–56	51–52	84–85
86–87	92–93	62–63	80–81	70–71	64–65
67–68	55–56	66–67	85–86	87–88	74–75
66–67	63–64	78–79	71–72	62–63	95–96
71–72	72–73	74–75	89–90	**57–58**	55–56
68–69	52–53	63–64	64–65	61–62	78–79
92–93	54–55	72–73	51–52	56–57	80–81
59–60	81–82	65–66	61–62	**73–74**	79–80
75–76	64–65	79–80	78–79	53–54	56–57
61–62	74–75	69–70	84–85	77–78	71–72
94–95	53–54	77–78	79–80	71–72	66–67
79–80	59–60	96–97	74–75	55–56	62–63
83–84	56–57	80–81	81–82	64–65	83–84
52–53	66–67	55–56	90–91	80–81	67–68
62–63	**88–89**	50–51	53–54	68–69	63–64
54–55	87–88	56–57	96–97	78–79	85–86
88–89	93–94	89–90	62–63	95–96	54–55
82–83	69–70	85–86	56–57	54–55	89–90
84–85	85–86	**57–58**	66–67	60–61	81–82
49–50	62–63	**88–89**	63–64	58–59	**57–58**
90–91	50–51	61–62	83–84	96–97	51–52
74–75	**91–92**	81–82	68–69	67–68	68–69
96–97	90–91	64–65	92–93	84–85	69–70
69–70	94–95	67–68	54–55	72–73	87–88
65–66	68–69	71–72	67–68	83–84	52–53
76–77	71–72	70–71	65–66	65–66	90–91
60–61	67–68	83–84	77–78	**97–98**	65–66
53–54	76–77	92–93	69–70	76–77	77–78
72–73	89–90	86–87	58–59	89–90	61–62
97–98	78–79	60–61	**57–58**	**82–83**	58–59
51–52	84–85	58–59	87–88	69–70	76–77
56–57	70–71	93–94	76–77	85–86	93–94
89–90	58–59	**91–92**	**91–92**	93–94	**91–92**
63–64	96–97	90–91	94–95	90–91	**97–98**
85–86	61–62	84–85	72–73	86–87	92–93
70–71	**97–98**	54–55	86–87	81–82	72–73
57–58	49–50	**97–98**	93–94	94–95	94–95
87–88	75–76	76–77	**97–98**	**91–92**	86–87
91–92	60–61	**82–83**	**82–83**	92–93	**82–83**

distribution function defined earlier. Table 4a shows the parameters (location, scale, and shape) of the fits to the GEV PDF for the six leading PCs. We see that all fits to the six leading PCs include a significant shape parameter. In fact, all of the estimated shape parameters are negative, indicating that the appropriate distribution is the reverse Weibull distribution. The 20-yr return values range from 5.3 standard deviations for the NW storms to about nine standard deviations for the TL and GC storms. This again highlights the high intensity of the extreme GC and TL storms as measured in terms of their typical daily variability.

We next examine the extent to which ENSO events impact the simulated EV statistics. The results (Table 4b) show substantial impacts of ENSO especially on the mean values for EC, TL, and GC storms. The impact is strongest for the EC and GC storms, with El Niño years producing more intense (larger amplitude) storms. There is also some tendency for the scale parameter to be affected by ENSO such that warm years tend to have more variability in the extremes. There is also some impact from ENSO on the other PCs. For example, ENSO impacts the parameters of the MW storms, though the impact comes primarily from the warm years (less so for the cold years). Both the TL and the MW distributions have shape parameters that are influenced by ENSO.

The last column in Table 4b shows the effective return values during warm, cold, and neutral years (see section 3c). We see only modest or no impacts of ENSO on the return values for the NW, WC, and MW storms (despite the impact on the individual parameters of the MW storm noted above). The return values for the EC storm is such that the 20-yr return value based on all years would occur on average in half that time during warm years and twice that time during cold years. The impact on the TL storm is such that the 20-yr return value would occur in about half that time during warm years and in almost quadruple that time (76 yr) during cold years. For the GC storm the 20-yr return value would also occur in half that time (10 yr) under warm conditions and in about 30 years under cold conditions.

We next compare the observed and simulated results for the EC and GC storms. As we saw earlier, these are the two storms that have clear counterparts in the observations and simulations. The top panel of Fig. 10 shows the results of fitting Gumbel distributions to the maxima of the GC storms separately for the warm and cold years for the observations and each of the nine ensemble members. We note that, before doing the fit of the maxima to the Gumbel distribution, the daily PC values are scaled so that the observed and simulated daily values have the same total variance: this is done because the simulated PCs have less variance than the observed. We choose here to fit the simpler Gumbel distribution to the model results since, by doing the fits to the individual ensemble members, we are limiting the sample size to that of the observations. The scatter among the ensemble members gives an indication of the sampling errors. The fact that the fit to the obser-

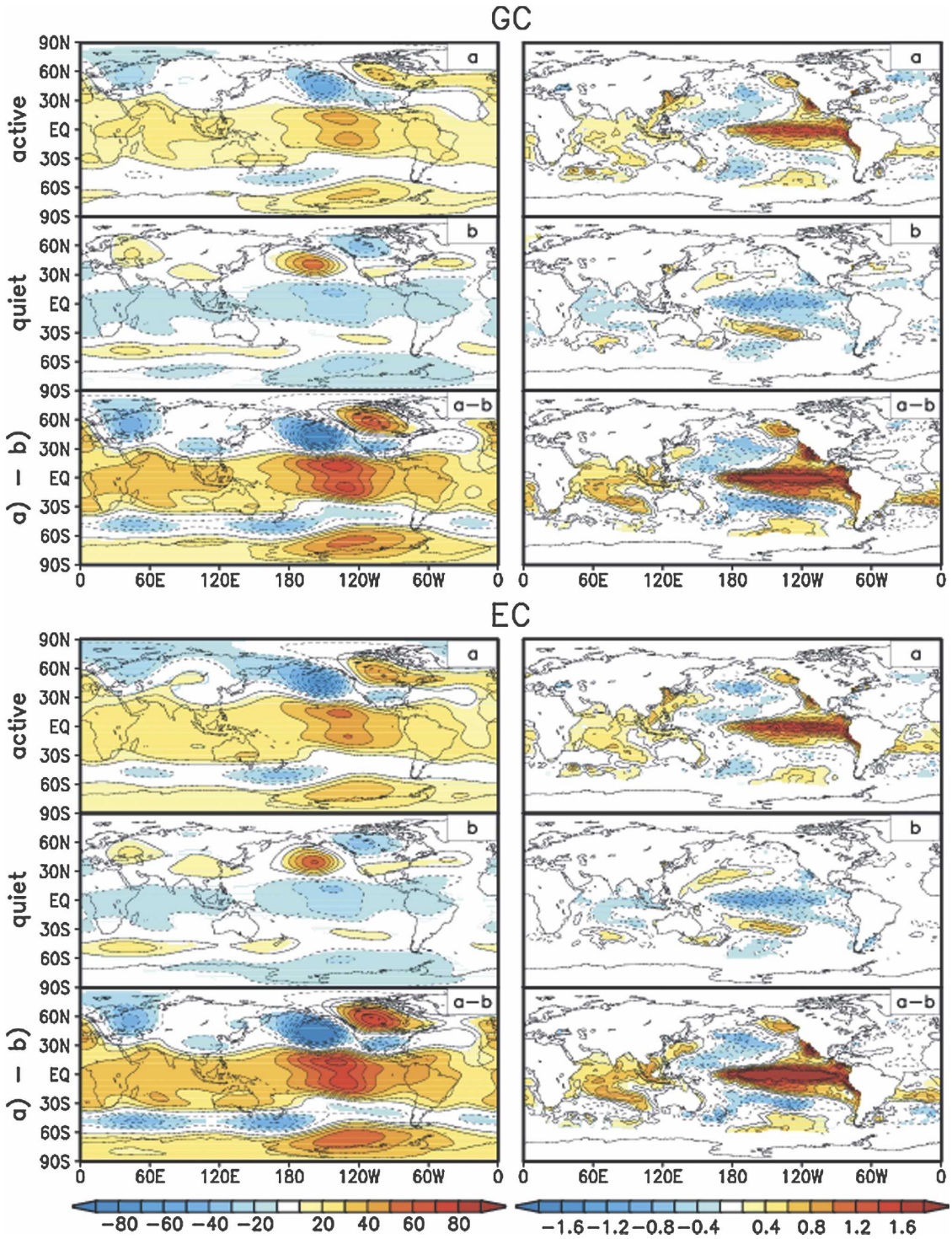

FIG. 9. As in Fig. 4, except for the results from the NSIPP-1 AGCM simulations. The years used in the composites are listed in Table 3.

vations falls within the scatter suggests that the model results are quite realistic. The results also show that the impact from ENSO clearly separates the warm and cold years (despite the sampling errors) with La Niña years tending to produce considerably less intense extremes than the El Niño years.

The bottom panel of Fig. 10 is the same as the top panel except it is for the EC storms. Here again we see

TABLE 4a. The parameter estimates of the GEV distribution for the six leading PCs from the model simulations. Values are based on the maximum daily values during DJF for the 441 winters composed of nine ensemble members multiplied by 49 (1949/50–1997/98) winters. Values in parentheses are the standard errors. The last column shows the 20-yr return values in units of standard deviation.

PC	μ	σ	ζ	X_{20}
1 (NW)	2.31 (0.03)	0.61 (0.02)	−0.16 (0.03)	5.3
2 (WC)	2.30 (0.04)	0.75 (0.03)	−0.21 (0.03)	5.9
3 (MW)	2.34 (0.04)	0.82 (0.03)	−0.17 (0.03)	8.0
4 (EC)	2.28 (0.04)	0.79 (0.03)	−0.07 (0.02)	8.3
5 (TL)	2.22 (0.05)	0.92 (0.03)	−0.10 (0.03)	8.8
6 (GC)	2.18 (0.05)	0.95 (0.04)	−0.14 (0.04)	8.9

that the fits to the observed values fall within the scatter of the fits to the individual ensemble members. The cold and warm years are also clearly separated, though in this case there is considerably more scatter in the results for the warm years, with some ensemble members showing a quite broad distribution while others are more narrow and peaked.

TABLE 4b. The parameter estimates of the GEV distribution for the six leading PCs from the model simulations. Values are based on the maximum daily values during DJF for the 441 winters composed of nine ensemble members times 49 (1949/50–1997/98) winters. Separate fits are done for La Niña, neutral, and El Niño winters. Values in parentheses are the standard errors. The last column shows the effective return period (in years) that the X_{20} value (obtained from the entire record; see Table 4a) would have under warm, cold, or neutral ENSO conditions. See text for details.

PC	ENSO	μ	σ	ζ	N^*
1 (NW)	Cold	2.19 (0.07)	0.63 (0.05)	−0.19 (0.07)	28
	Neutral	2.31 (0.05)	0.59 (0.03)	−0.15 (0.03)	21
	Warm	2.40 (0.06)	0.59 (0.04)	−0.15 (0.06)	17
2 (WC)	Cold	2.28 (0.07)	0.70 (0.05)	−0.12 (0.07)	18
	Neutral	2.37 (0.06)	0.77 (0.04)	−0.26 (0.05)	20
	Warm	2.24 (0.07)	0.77 (0.05)	−0.23 (0.06)	24
3 (MW)	Cold	2.24 (0.07)	0.70 (0.05)	−0.12 (0.05)	34
	Neutral	2.31 (0.06)	0.77 (0.05)	−0.08 (0.05)	17
	Warm	2.47 (0.09)	0.93 (0.06)	−0.30 (0.04)	18
4 (EC)	Cold	2.02 (0.07)	0.71 (0.05)	−0.06 (0.05)	43
	Neutral	2.19 (0.06)	0.73 (0.04)	−0.04 (0.04)	26
	Warm	2.68 (0.08)	0.84 (0.05)	−0.10 (0.03)	11
5 (TL)	Cold	2.07 (0.09)	0.86 (0.06)	−0.20 (0.06)	76
	Neutral	2.20 (0.07)	0.86 (0.05)	−0.12 (0.04)	28
	Warm	2.44 (0.10)	1.04 (0.07)	−0.01 (0.07)	8.4
6 (GC)	Cold	1.72 (0.08)	0.80 (0.06)	−0.04 (0.08)	33
	Neutral	2.19 (0.07)	0.90 (0.05)	−0.16 (0.05)	28
	Warm	2.64 (0.09)	0.96 (0.06)	−0.15 (0.06)	10

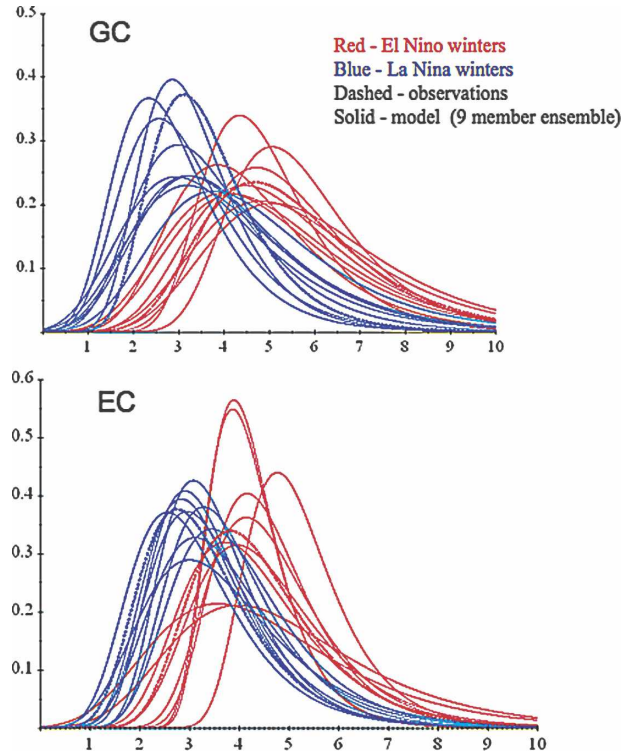

FIG. 10. PDFs of extreme winter storms that form in the Gulf of Mexico (GC) and along the East Coast (EC) for the period 1949–98. The GC PDFs correspond to the maximum value of the principal components associated with EOF 3 (observations) and EOF 6 (model). The EC PDFs correspond to the maximum value of the principal components associated with EOF 4 for both observations and model. The PDFs are the fits to a Gumbel distribution. PDFs from the observations are dashed. Values are scaled so that the model and observed EOFs have the same total variance. Units are arbitrary. The PDFs are the fits to a Gumbel distribution.

5. Summary and conclusions

In this study we examined the impact of ENSO on wintertime precipitation events over the continental United States using 49 winters (1949/50–1997/98) of daily precipitation observations and NCEP–NCAR reanalyses. The results were compared with those from an ensemble of nine AGCM simulations forced with observed SST for the same time period. EOFs of the daily precipitation fields together with compositing techniques were used to identify and characterize the weather systems that dominate the winter precipitation variability. The time series of the PCs associated with the leading EOFs were analyzed using generalized extreme value distributions to quantify the impact of ENSO on the intensity of extreme precipitation events.

The six leading EOFs of the observations represent major winter storm systems and account for more than 50% of the daily precipitation variability along the

West Coast and over much of the eastern part of the country. Two of the leading EOFs (designated GC for Gulf Coast and EC for East Coast) together represent cyclones that develop in the Gulf of Mexico and occasionally move and/or redevelop along the East Coast producing large amounts of precipitation over much of the southern and eastern United States. Three of the leading EOFs represent storms that hit different sections of the West Coast (designated SW for Southwest coast, WC for the central West Coast, and NW for Northwest coast), while another represents storms that affect the Midwest (designated by MW).

An assessment of the overall activity (daily variance) of the storms for each year shows a clear predilection for enhanced storm activity during El Niño winters for the GC, EC, and SW storms and a suppression of GC storm activity during La Niña years. Composites of the 300-mb height and SST anomalies associated with the 10 most active and the 10 least active years for each storm highlight the important role of ENSO in modulating the large-scale storm environment. An extreme value analysis shows that the impact on storm intensity (PC amplitude) is such that GC, EC, and SW storms that occur on average only once every 20 years (20-yr storms) would occur on average in half that time under sustained El Niño conditions. In contrast, under La Niña conditions, 20-yr GC and EC storms would occur on average about once in 30 years, while there is little impact of La Niña on the intensity of the SW storms.

The leading EOFs from the model simulations and their connections to ENSO are for the most part quite similar to those from the observations. The main model deficiencies are the lack of SW storms and an overall underestimate of the daily precipitation variance. It is likely that the coarse model resolution (typical of climate models) contributes to the latter, while we speculate that the lack of a realistic MJO may contribute to the former. An overall assessment of the activity of the storms shows that the model has a similar predilection for enhanced storminess during El Niño and suppressed storminess during La Niña years. The model, in particular, does quite well in reproducing the impact of ENSO on the intensity of EC and GC storms. The enhanced sample size offered by the simulations provides greater confidence in the ENSO–weather connections. It also allowed a more refined fit to the GEV distributions to reveal that the reverse Weibull distribution is generally a better fit to the extreme values than the simpler Gumbel distribution.

Acknowledgments. This work was supported by the NASA Earth Science Enterprise's Global Modeling and Analysis Program.

REFERENCES

Bacmeister, J., P. J. Pegion, S. D. Schubert, and M. J. Suarez, 2000: An atlas of seasonal means simulated by the NSIPP 1 atmospheric GCM. NASA Goddard Space Flight Center Tech. Memo 104606, Vol. 17, 218 pp.

Bell, G. D., and W. Higgins, 2005: U.S. storms and flooding in the West and Midwest: Exceptional warmth in the Midwest and East. NOAA Climate Prediction Center/NWS/NCEP Rep., 10 pp. [Available online at http://www.cpc.ncep.noaa.gov/products/expert_assessment/california_assessment_2005.pdf.]

Cayan, D. R., K. T. Redmond, and L. G. Riddle, 1999: ENSO and hydrological extremes in the western United States. *J. Climate,* **12,** 2881–2893.

Chou, M.-D., and M. J. Suarez, 1994: An efficient thermal infrared radiation parameterization for use in general circulation models. NASA Goddard Space Flight Center Tech. Memo 104606, Vol. 3, 85 pp.

——, and ——, 2000: A solar radiation parameterization for atmospheric studies. NASA Goddard Space Flight Center Tech. Memo 104606, Vol. 11, 40 pp.

Coles, S., 2001: *An Introduction to Statistical Modeling of Extreme Values*. Springer-Verlag, 208 pp.

Gershunov, A., 1998: ENSO influence on intraseasonal extreme rainfall and temperature frequencies in the contiguous United States: Implications for long-range predictability. *J. Climate,* **11,** 3192–3203.

——, and T. P. Barnett, 1998: ENSO influence on intraseasonal extreme rainfall and temperature frequencies in the contiguous United States: Observations and model results. *J. Climate,* **11,** 1575–1586.

Helfand, M., and S. D. Schubert, 1995: Climatology of the simulated Great Plains low-level jet and its contribution to the continental moisture budget of the United States. *J. Climate,* **8,** 784–806.

Higgins, R. W., J. E. Janowiak, and Y. Yao, 1996: *A Gridded Hourly Precipitation Database for the United States (1963–93)*. NOAA/NWS/NCEP/Climate Prediction Center Atlas No. 1, 47 pp.

——, Y. Yao, E. S. Yarosh, J. E. Janowiak, and K. C. Mo, 1997: Influence of the Great Plains low-level jet on the summertime precipitation and moisture transport over the central United States. *J. Climate,* **10,** 481–507.

——, J.-K. Schemm, W. Shi, and A. Leetmaa, 2000: Extreme precipitation events in the western United States related to tropical forcing. *J. Climate,* **13,** 793–820.

Hoerling, M. P., and A. Kumar, 1997: Origins of extreme climate states during the 1982–83 ENSO winter. *J. Climate,* **10,** 2859–2870.

Houghton, J. T., Y. Ding, D. J. Griggs, M. Noguer, P. J. van der Linden, and D. Xiaosu, Eds., 2001: *Climate Change 2001: The Scientific Basis*. Cambridge University Press, 881 pp.

Kalnay, E., and Coauthors, 1996: The NCEP/NCAR 40-Year Reanalysis Project. *Bull. Amer. Meteor. Soc.,* **77,** 437–471.

Katz, R. W., M. B. Parlange, and P. Naveau, 2002: Statistics of extremes in hydrology. *Adv. Water Resour.,* **25,** 1287–1304.

Koster, R. D., and M. J. Suarez, 1996: Energy and water balance calculations in the Mosaic LSM. NASA Tech. Memo 104606, Vol. 9, 194 pp.

Louis, J., M. Tiedtke, and J. Geleyn, 1982: A short history of the PBL parameterization at ECMWF. *Proc. ECMWF Work-*

shop on Planetary Boundary Layer Parameterization, Reading, United Kingdom, ECMWF, 59–80.

Mo, K., 1999: Alternating wet and dry episodes over California and intraseasonal oscillations. *Mon. Wea. Rev.,* **127,** 2759–2776.

——, and R. W. Higgins, 1998: Tropical influences on California precipitation. *J. Climate,* **11,** 412–430.

Moorthi, S., and M. J. Suarez, 1992: Relaxed Arakawa–Schubert: A parameterization of moist convection for general circulation models. *Mon. Wea. Rev.,* **120,** 978–1002.

Noel, J., and D. Changnon, 1998: A pilot study examining U.S. winter cyclone frequency patterns associated with three ENSO parameters. *J. Climate,* **11,** 2152–2159.

Pegion, P. J., S. D. Schubert, and M. J. Suarez, 2000: An assessment of the predictability of northern winter seasonal means with the NSIPP 1 AGCM. Goddard Space Flight Center NASA Tech. Memo 104606, Vol. 18, 124 pp.

Reiss, R.-D., and M. Thomas, 1997: *Statistical Analysis of Extreme Values*. Birkhäuser, 316 pp.

Schonher, T., and S. E. Nicholson, 1989: The relationship between California rainfall and the ENSO events. *J. Climate,* **2,** 1258–1269.

Schubert, S. D., H. M. Helfand, C.-Y. Wu, and W. Min, 1998: Subseasonal variations in warm-season moisture transport and precipitation over the central and eastern United States. *J. Climate,* **11,** 2530–2555.

——, M. J. Suarez, P. J. Pegion, M. A. Kistler, and A. Kumer, 2002: Predictability of zonal means during boreal summer. *J. Climate,* **15,** 420–434.

Suarez, M. J., and L. L. Takacs, 1995: Documentation of the Aries-GEOS Dynamical Core: Version 2. Goddard Space Flight Center NASA Tech. Memo 104606, Vol. 5, 56 pp.

Webb, R. H., and J. L. Betancourt, 1992: Climate variability and flood frequency of the Santa Cruz River, Pima County, Arizona. U.S. Geological Survey Water-Supply Paper 2379, 40 pp.

Whittaker, L. M., and L. H. Horn, 1984: Northern Hemisphere extratropical cyclone activity for four mid-season months. *J. Climatol.,* **4,** 297–310.

Yarnal, B., and H. F. Diaz, 1986: Relationships between extremes of the southern oscillation and the winter climate of the Anglo-American Pacific Coast. *J. Climatol.,* **6,** 197–219.

Zwiers, F. W., and V. V. Kharin, 1998: Changes in the extremes of the climate simulated by CCC GCM2 under CO2 doubling. *J. Climate,* **11,** 2200–2222.